Hybrid Gaussian–discrete-variable representation approach to molecular continuum processes: Application to photoionization of diatomic Li$_2^+$

F. L. Yip,[1,2] C. W. McCurdy,[2,3] and T. N. Rescigno[2]

[1]*Department of Chemistry, University of California, Berkeley, California 94720, USA*
[2]*Lawrence Berkeley National Laboratory, Chemical Sciences, Berkeley, California 94720, USA*
[3]*Departments of Applied Science and Chemistry, University of California, Davis, California 95616, USA*

We describe an approach for studying molecular photoionization with a hybrid basis that combines the functionality of analytic basis sets to represent electronic coordinates near the nuclei of a molecule with numerically defined grid-based functions. We discuss the evaluation of the various classes of two-electron integrals that occur in a hybrid basis consisting of Gaussian-type orbitals and discrete-variable representation functions. This combined basis is applied to calculate single photoionization cross sections for molecular Li$_2^+$, which has a large equilibrium bond distance ($R=5.86a_0$). The highly nonspherical nature of Li$_2^+$ molecules causes higher angular momentum components to contribute significantly to the cross section even at low photoelectron energies, resulting in angular distributions that appear to be *f*-wave dominated near the photoionization threshold. At higher energies, where the de Broglie wavelength of the photoelectron becomes comparable with the bond distance, interference effects appear in the photoionization cross section. These interference phenomena appear at much lower energies than would be expected for diatomic targets with shorter internuclear separations.

PACS number(s): 33.80.Eh

I. INTRODUCTION

Complete *ab initio* treatments of photodouble ionization processes have previously been limited to the simplest atoms [1–5] and molecules [6–14], owing in large part to the complexity of representing a fully quantum mechanical system accurately both before and after the photon is absorbed. In particular, it is the representation of the final-state wave function for processes that eject two electrons into the continuum that presents the greatest computational challenge. In contrast to the initially bound state for either an atomic or molecular target, the wave function for double ionization requires consideration of electron-electron interactions over relatively large distances because of the long-range Coulomb forces inherent to the problem [15,16]. The evaluation of fully differential cross sections requires accurate computation of these final continuum states to reveal the full photoionization picture.

Several different methods have been developed to compute double photoionization cross sections extracted from various treatments of the final continuum states [17–24]. One such method involves a compact support basis incorporating exterior complex scaling to treat the radial coordinates of the electrons on a finite grid [25]. The angular degrees of freedom of each electron in such a single-center description are represented by spherical harmonics. These methods have proven to be extremely successful for both simple atoms [2–5] and molecules [11–14].

In principle, this framework can be adapted beyond the cases considered to be able to treat more complex molecules, but in practice the limitations of describing both the bound and continuum states of the target molecule using a single-center expansion are quickly realized. Unlike the atomic case where radial-angular product bases are well suited for expanding the wave function about the nucleus, the nonspherical symmetry of molecules couples the various partial waves.

This limitation is such that converged treatments of molecular double photoionization expanded about the origin have only been reported for H$_2$ and H$_2^+$. The ultimate goal of being able to probe electron correlation in a molecule with N electrons would require a computational framework beyond these existing methods as convergence issues render the problem increasingly intractable. Considering the wealth of information potentially unlocked from being able to conduct an investigation of double photoionization from an N-electron molecule, including the ability to probe correlation within and between the different molecular orbitals, the existing framework for describing these complex systems must be advanced.

Previously, we reported on a method [14], referred to hereafter as paper I, that offers a possible avenue for considering more general molecular photoionization problems beyond the cases that have been illustrated to date. This method distinguishes between the regions of space near the nuclei where most of the electron probability density lies for a molecular bound state and a region just beyond the nuclei where bound state functions fall off exponentially while continuum states oscillate as outgoing waves. By partitioning the physical space into these regions and allowing for some common intersection for the basis functions that span each area to connect the two, the representation of the wave function becomes compartmentalized according to which type of basis function is best suited for describing each region. The motivation for what we have called the "hybrid basis" lies in combining the well-tested technologies involved in both computing molecular wave functions bounded near the nuclei and representing oscillating outgoing wave functions far from the nuclei using a grid-based scheme.

The utility of the hybrid method was previously demonstrated in paper I with illustrative examples involving the hydrogen molecular ion H$_2^+$. The hybrid method was shown

to provide accurate results using less computational resources than a pure grid-based approach to the problem by avoiding the single-center expansion limitations around the nuclei as discussed above. The ultimate goal of evolving the hybrid method to be able to treat double ionization in multi-electron molecular targets requires the development of efficient methods for computing electron-electron repulsion integrals in a mixed basis representation. In the present work we investigate the various classes of two-electron integrals that arise and provide a framework for their computation with illustrative calculations of single photoionization of the Li_2^+ molecule, which has one valence electron outside a closed-shell core. The interaction of the valence electron with the four core electrons requires the evaluation of two-electron integrals in the mixed hybrid basis framework. In addition, the Li_2^+ molecule provides an interesting case to study in its own right. With an equilibrium bond distance of nearly 6 bohr, Li_2^+ represents a highly nonspherical molecular system. The large internuclear separation, compared to other covalently bonded diatomics, would require many coupled partial waves to expand the wave function about the bonding midpoint, which is impractical in a pure grid-based framework. By utilizing traditional quantum chemistry descriptions within this internuclear region, the hybrid basis representation can avoid these complications that plague pure grid-based partial wave expansions of molecular targets with severely nonspherical nuclear geometries.

In Sec. II we discuss the theoretical framework for the hybrid basis with exterior complex scaling. Section II B provides a brief review of the hybrid basis construction as described in paper I. Section II C catalogues the various classes of two-electron integrals that occur in the hybrid basis framework and elaborates on their evaluation. Section III details the construction of the Hamiltonian for Li_2^+. Section IV illustrates the hybrid method by computing bound state eigenvalues of Li_2^+. Section V describes the contiuum state description and evaluation, with illustative examples of the method used to compute photoionization cross sections in Sec. VI. A brief conculsion follows in Sec. VII.

II. FORMULATION OF A MULTIELECTRON HYBRID REPRESENTATION

A. Continuum wave-function treatment using exterior complex scaling

One method of addressing the computation of atomic and molecular states involving continuum electrons has been to utilize exterior complex scaling (ECS) [26,27]. Under ECS, the radial coordinate of each electron is rotated into the complex plane beyond some value r_{ECS},

$$r \rightarrow \begin{cases} r, & r \leq r_{ECS}, \\ r_{ECS} + (r - r_{ECS})e^{i\eta}, & r > r_{ECS}. \end{cases} \quad (1)$$

Such a transformation causes oscillatory wave functions with any number of outgoing electrons to decrease exponentially in the complex scaled region beyond r_{ECS}, thereby permitting the physical process to be described over a finite volume. Inside of the complex scaling radius, however, the wave
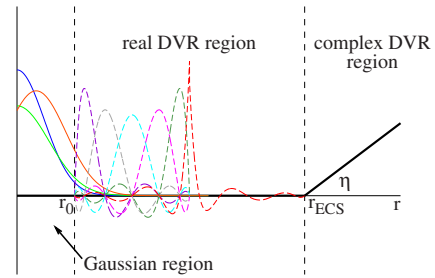

FIG. 1. (Color online) Division of the radial coordinate in the hybrid method. Only Gaussians are nonzero inside of r_0. The tails of the diffuse Gaussians extend into the real DVR region. Near the complex scaling turning point r_{ECS} only the DVR functions are nonzero.

function is the physical wave function containing the full information of the outgoing state. The details of exterior complex scaling, including the interrogation of the wave function just inside of the complex region to evaluate physically relevant amplitudes desciribing electrons leaving the target are more fully discussed in a recent paper [25]. The ECS method has been successfully demonstrated for both atoms and molecular targets with one or two electrons placed into the continuum.

B. Hybrid Gaussian–DVR basis representation

The basic idea of the hybrid method, as outlined in paper I, is to divide physical space into three parts: An interior region bounded by a sphere of radius r_0, which encloses all the nuclei, an intermediate region which extends to r_{ECS} and an outer (complex) region that extends to a terminal radius r_{max}. Each region is distinguished by the types of functions that primarily exist within them. The basic principles of combining the two unique basis function types to produce a hybrid basis are illustrated in Fig. 1. Within the inner region $0 \leq r < r_0$, the wave function is described exclusively by Gaussian functions which can be centered arbitrarily within the inner sphere. A product basis of radial, grid-based polynomial functions multiplied by spherical harmonics spans the region bounded by spheres of inner radius r_0 and outer radius r_{max},

$$\chi_i^{lm}(\mathbf{r}) = \frac{\phi_i(r)}{r} Y_{l,m}(\hat{\mathbf{r}}). \quad (2)$$

Beyond r_{ECS}, which lies between r_0 and r_{max}, the radial functions are complex. The polynomial functions have compact support and are only defined between r_0 and r_{max}. These functions are constructed using a discrete-variable representation employing finite elements (FEM-DVR) and ECS [28].

The inner and outer regions are connected by Gaussian functions which extend into the intermediate region, as demonstrated in Fig. 1. The Gaussian-type orbitals (GTOs) are all assumed to be zero beyond r_{ECS}. We use "contracted" Gaussian basis functions, which are simply linear combinations of Cartesian functions, centered at $\mathbf{R}_\Gamma = (X_\Gamma, Y_\Gamma, Z_\Gamma)$, of the form

$$G_\Gamma(\mathbf{r}) = N_\Gamma(x - X_\Gamma)^{l_\Gamma}(y - Y_\Gamma)^{m_\Gamma}(z - Z_\Gamma)^{n_\Gamma}e^{-\alpha_\Gamma|\mathbf{r} - \mathbf{R}_\Gamma|^2}, \quad (3)$$

where Γ labels each "primitive" basis function and N_Γ is a normalization constant. This choice is a standard in most molecular electronic structure codes [29].

Because of the partitioning of physical space according to Fig. 1, we can use a relatively small number of Gaussian basis functions in the hybrid Gaussian–DVR basis construction. The ability of the FEM–DVR to essentially completely span the space beyond the nuclei obviates the need for diffuse GTOs. Moreover, by appropriately choosing the orbital exponents α_Γ in Eq. (3) and placing the ECS rotation point sufficiently far from the nuclei to guarantee that the GTOs have decayed before r_{ECS}, matrix elements between GTO and DVR functions defined on the complex contour need not be considered. In fact, the Gaussian basis function extent and number of real finite elements for which mixed matrix elements are nonzero by design is flexible, subject to the maintenance of linear dependence, on the one hand, and an adequate connection between the two regions, on the other.

The discrete-variable representation [30] of the radial coordinate employs a grid defined by a numerical Gauss-Lobatto quadrature [31]. The associated radial basis functions provide an underlying continuous representation of the wave function while possessing the property of discrete orthonormality at the quadrature points,

$$\phi_i(r_j) = \delta_{i,j}/\sqrt{w_i}. \quad (4)$$

Thus, the functions provide a diagonal representation of any local operator evaluated under Gauss-Lobatto quadrature,

$$\int_a^b \phi_i(r)V(r)\phi_j(r)dr \approx \sum_{k=1}^n \phi_i(r_k)V(r_k)\phi_j(r_k)w_k = V(r_i)\delta_{i,j}. \quad (5)$$

The implementation of this DVR scheme with finite elements facilitates the incorporation of exterior complex scaling by permitting the border point r_{ECS} to be placed at a finite element boundary [28]. Additionally, the location of the first finite element boundary r_0 and flexible control over the Gaussian–DVR overlap region can also be exercised with this method.

C. Matrix element evaluation in the hybrid representation

Matrix elements in the hybrid method can be grouped into three categories: (1) Those that involve only Gaussian basis functions $G_\Gamma(\mathbf{r})$, (2) those that involve only grid-based functions $\chi_i^{lm}(\mathbf{r})$ and finally, (3) those that involve both $G_\Gamma(\mathbf{r})$ and $\chi_i^{lm}(\mathbf{r})$. The evaluation of integrals involving only Gaussians is an established part of electronic structure theory [32] and there is no need to discuss the subject here. The various one-electron integrals (overlap, kinetic energy and nuclear attraction) are accurately calculated using Lobatto or Legendre quadrature for the radial coordinate and a high-order Gauss-Markov angular quadrature [33], as outlined in paper I. In many-electron problems, the majority of the work goes into computing four-index two-electron integrals that arise from the electron-electron repulsion,

$$\langle ij\|kl\rangle \equiv \int \phi_i^\dagger(\mathbf{r}_1)\phi_j^\dagger(\mathbf{r}_2)\frac{1}{r_{12}}\phi_k(\mathbf{r}_1)\phi_l(\mathbf{r}_2)d\mathbf{r}_1 d\mathbf{r}_2, \quad (6)$$

where $r_{12} = |\mathbf{r}_1 - \mathbf{r}_2|$. The notation $\phi^\dagger(\mathbf{r})$ indicates complex conjugation, but only of angular functions. The Gaussian functions are real in any case; the grid-based functions are products of radial DVR functions, which are evaluated on the (complex) ECS grid and used without complex conjugation [25], and spherical harmonics which are complex conjugated.

The various classes of two-electron integrals encountered in the hybrid Gaussian–DVR scheme are considered in some detail below. In what follows, Gaussian basis functions are denoted $G_i(\mathbf{r})$ and DVR basis functions are denoted $\chi_j^a(\mathbf{r}) = r^{-1}\phi_j(r)Y_{l^a,m^a}(\hat{\mathbf{r}})$.

1. Class 1 integrals: $\langle G_iG_j|G_k\chi_l^d\rangle$ and $\langle G_i\chi_j^b|G_k\chi_l^d\rangle$

The class of integrals involving either three GTOs or two GTOs with the same electron coordinate are evaluated by first carrying out the electron repulsion integral

$$I_{i,k}(\mathbf{r}_2) \equiv \int G_i(\mathbf{r}_1)\frac{1}{r_{12}}G_k(\mathbf{r}_1)d\mathbf{r}_1, \quad (7)$$

to give a local potential that is a function of the second electron coordinates. This integral can be done analytically [32]. The integration over the remaining electron coordinate is done by quadrature. In both cases, the discrete orthonormality of the radial DVR functions under Gauss-Lobatto quadrature [Eq. (4)] reduces the integration to an angular quadrature over the surface of a sphere, which is efficiently handled using Gauss-Markov quadrature [33]:

$$\langle G_iG_j|G_k\chi_l^d\rangle = r_l\sqrt{w_l}\int I_{i,k}(r_l;\hat{\mathbf{r}}_2)G_j(r_l;\hat{\mathbf{r}}_2)Y_{\ell^d,m^d}(\hat{\mathbf{r}}_2)d\hat{\mathbf{r}}_2. \quad (8)$$

$$\langle G_i\chi_j^b|G_k\chi_l^d\rangle = \delta_{j,l}\int I_{i,k}(r_j;\hat{\mathbf{r}}_2)Y_{\ell^b,m^b}^*(\hat{\mathbf{r}}_2)Y_{\ell^d,m^d}(\hat{\mathbf{r}}_2)d\hat{\mathbf{r}}_2. \quad (9)$$

2. Class 2 integrals: $\langle \chi_i^a\chi_j^b|\chi_k^c\chi_l^d\rangle$ and $\langle G_i\chi_j^b|\chi_k^c\chi_l^d\rangle$

The evaluation of these integrals follows a general scheme that we outlined in our recent paper [25], with modifications needed to accommodate an FEM-DVR that begins at an arbitrary r_0. We represent the electron-electron repulsion as a multipole expansion,

$$\frac{1}{r_{12}} = \sum_{\lambda,\mu}\frac{4\pi}{2\lambda + 1}Y_{\lambda,\mu}(\hat{\mathbf{r}}_1)\frac{r_<^\lambda}{r_>^{\lambda+1}}Y_{\lambda,\mu}^*(\hat{\mathbf{r}}_2). \quad (10)$$

We first integrate over the electron coordinate shared by two DVR functions,

$$\int \frac{\phi_j(r_2)}{r_2} \frac{\phi_l(r_2)}{r_2} \frac{r_<^\lambda}{r_>^{\lambda+1}} Y_{\ell^d,m^d}(\hat{\mathbf{r}}_2) Y_{\ell^b,m^b}^*(\hat{\mathbf{r}}_2) Y_{\lambda,\mu}^*(\hat{\mathbf{r}}_2) d\mathbf{r}_2$$

$$= C(l^d m^d | l^b m^b, \lambda\mu) \int_{r_0}^{r_{max}} \phi_j(r_2) \phi_l(r_2) \frac{r_<^\lambda}{r_>^{\lambda+1}} dr_2$$

$$\equiv C(l^d m^d | l^b m^b, \lambda\mu) U_{j,l}^\lambda(r_1), \quad (11)$$

where the angular integral,

$$C(l^d m^d | l^b m^b, \lambda\mu) = \int Y_{\ell^d,m^d}(\hat{\mathbf{r}}_2) Y_{\ell^b,m^b}^*(\hat{\mathbf{r}}_2) Y_{\lambda,\mu}^*(\hat{\mathbf{r}}_2) d\hat{\mathbf{r}}_2, \quad (12)$$

is well known from atomic spectroscopy [34]. Gauss-Lobatto quadrature cannot be used in the radial integral defining $U_{j,l}^\lambda(r_1)$ because of the derivative discontinuity in the potential $\frac{r_<^\lambda}{r_>^{\lambda+1}}$. However, we can restore the validity of the underlying Gauss quadrature by applying the DVR to solving an equivalent Poisson's equation for the potential due to the charge distribution corresponding to the product of the two radial DVR basis functions,

$$\left(\frac{d^2}{dr^2} - \frac{\lambda(\lambda+1)}{r^2}\right) r U_{j,l}^\lambda(r) = -\frac{2\lambda+1}{r} \phi_j(r)\phi_l(r), \quad (13)$$

along with the boundary conditions

$$U_{j,l}^\lambda(r_0) = \delta_{j,l} r_0^\lambda / r_j^{\lambda+1},$$

$$U_{j,l}^\lambda(r_{max}) = \delta_{j,l} r_j^\lambda / r_{max}^{\lambda+1}. \quad (14)$$

The general solution of Poisson's equation can be written as

$$r U_{j,l}^\lambda(r) = A r^{\lambda+1} + B/r^{-\lambda} + r U_{j,l}^{\lambda(0)}(r), \quad (15)$$

where A and B are coefficients of the two linearly independent solutions of the homogeneous equation, which are determined by the boundary conditions of Eq. (14) and $r U_{j,l}^{\lambda(0)}(r)$ is the particular solution that vanishes at the endpoints r_0 and r_{max}. We can obtain the particular solution by expanding that function in the FEM-DVR basis,

$$r U_{j,l}^{\lambda(0)}(r) = \sum_{m=1}^N C_m \phi_m(r). \quad (16)$$

Substituting this expansion into Eq. (13) gives an expression for the coefficients C_m,

$$C_m = (2\lambda+1) \frac{[T_{m,j}^{(\lambda)}]^{-1} \delta_{j,l}}{r_j \sqrt{w_j}}, \quad (17)$$

with $[T_{m,j}^{(\lambda)}]^{-1}$ denoting the m,j element of the inverse of the matrix

$$T_{n,m}^{(\lambda)} = -\int_0^{r_{max}} \phi_n(r)\left(\frac{d^2}{dr^2} - \frac{\lambda(\lambda+1)}{r^2}\right)\phi_m(r) dr. \quad (18)$$

Equations (15)–(17), along with Eq. (14), are combined to obtain

$$r U_{j,l}^\lambda(r) = \delta_{j,l}\left[(2\lambda+1)\sum_{m=1}^N \frac{\phi_m(r)}{r_j\sqrt{w_j}} [T_{m,j}^{(\lambda)}]^{-1} + \left(\frac{r_0^{2\lambda+1}}{r_0^{2\lambda+1} - r_{max}^{2\lambda+1}}\right)\right.$$

$$\left.\times \left(\frac{r^{\lambda+1}}{r_j^{\lambda+1}} + \frac{r_j^\lambda}{r^\lambda} - \frac{r^{\lambda+1}r_j^\lambda}{r_0^{2\lambda+1}} - \frac{r_{max}^{2\lambda+1}}{r^\lambda r_j^{\lambda+1}}\right)\right]. \quad (19)$$

We can now complete the evaluation of the two-electron matrix elements by using the result above for $r U_{j,l}^\lambda$ and integrating over the coordinates of the remaining electron, using Gauss-Lobatto quadrature. The result for $\langle \chi_i^a \chi_j^b | \chi_k^c \chi_l^d \rangle$ is

$$\langle \chi_i^a \chi_j^b | \chi_k^c \chi_l^d \rangle = \sum_{\lambda=|\ell^a-\ell^c|}^{\ell^a+\ell^c} \frac{4\pi}{2\lambda+1} R_{i,j,k,l}^\lambda \sum_{\mu=-\lambda}^\lambda (-1)^\mu$$

$$\times C(\ell^c m^c | \ell^a m^a, \lambda\mu) C(\ell^d m^d | \ell^b m^b, \lambda-\mu), \quad (20)$$

where the radial factor $R_{i,j,k,l}^\lambda$ is given by

$$R_{i,j,k,l}^\lambda = \int_{r_0}^{r_{max}} \phi_i(r_1)\phi_j(r_2) \frac{r_<^\lambda}{r_>^{\lambda+1}} \phi_k(r_1)\phi_l(r_2) dr_1 dr_2$$

$$= \delta_{i,k}\delta_{j,l}\left[\frac{2\lambda+1}{r_i r_j \sqrt{w_i w_j}} [T_{i,j}^\lambda]^{-1} + \left(\frac{r_0^{2\lambda+1}}{r_0^{2\lambda+1} - r_{max}^{2\lambda+1}}\right)\left(\frac{r_i^\lambda}{r_j^{\lambda+1}}\right.\right.$$

$$\left.\left.+ \frac{r_j^\lambda}{r_i^{\lambda+1}} - \frac{r_i^\lambda r_j^\lambda}{r_0^{2\lambda+1}} - \frac{r_{max}^{2\lambda+1}}{r_i^{\lambda+1} r_j^{\lambda+1}}\right)\right]. \quad (21)$$

Similarly, for $\langle G_i \chi_j^b | \chi_k^c \chi_l^d \rangle$, the final working expression is

$$\langle G_i \chi_j^b | \chi_k^c \chi_l^d \rangle = \sum_{\lambda=|\ell^b-\ell^d|}^{\ell^b+\ell^d} \frac{4\pi}{2\lambda+1} U_{j,l}^\lambda(r_k)\left[\sum_{\mu=-\lambda}^\lambda C(\ell^d m^d | \ell^b m^b, \lambda\mu)\right.$$

$$\left.\times \left(\int G_i(r_k;\hat{\mathbf{r}}_1) Y_{\ell^c,m^c}(\hat{\mathbf{r}}_1) Y_{\lambda,\mu}(\hat{\mathbf{r}}_1) d\hat{\mathbf{r}}_1\right)\right], \quad (22)$$

where

$$U_{j,l}^\lambda(r_k) = \int \phi_j(r_2)\phi_l(r_2) \frac{r_<^\lambda}{r_>^{\lambda+1}} dr_2$$

$$= \delta_{j,l}\left[\frac{(2\lambda+1)}{r_k r_j \sqrt{w_k w_j}} [T_{k,j}^\lambda]^{-1} + \left(\frac{r_0^{2\lambda+1}}{r_0^{2\lambda+1} - r_{max}^{2\lambda+1}}\right)\right.$$

$$\left.\times \left(\frac{r_k^\lambda}{r_j^{\lambda+1}} + \frac{r_j^\lambda}{r_k^{\lambda+1}} - \frac{r_k^\lambda r_j^\lambda}{r_0^{2\lambda+1}} - \frac{r_{max}^{2\lambda+1}}{r_k^{\lambda+1} r_j^{\lambda+1}}\right)\right]. \quad (23)$$

The angular integration in Eq. (22) is again performed with Gauss-Markov quadrature.

3. Class 3 integrals: $\langle G_i G_j | \chi_k^c \chi_l^d \rangle$

The class of "exchange" integrals, where a Gaussian and DVR basis function are paired for each electron,

$$\langle G_i G_j | \chi_k^c \chi_l^d \rangle = \int \int G_i(\mathbf{r}_1) G_j(\mathbf{r}_2) \frac{1}{r_{12}} \chi_k^c(\mathbf{r}_1) \chi_l^d(\mathbf{r}_2) d\mathbf{r}_1 d\mathbf{r}_2. \tag{24}$$

are the most difficult to evaluate. The strategy here is to construct a single-center expansion of the product of a Gaussian and the spherical harmonic part of the DVR function,

$$r G_i(\mathbf{r}) Y_{l',m'}(\hat{\mathbf{r}}) = \sum_{l,m} R_{l,m}^{i,l',m'}(r) Y_{l,m}(\hat{\mathbf{r}}), \tag{25}$$

with expansion coefficients defined as

$$R_{l,m}^{i,l',m'}(r) = r \int G_i(\hat{\mathbf{r}}; r) Y_{l',m'}(\hat{\mathbf{r}}) Y_{l,m}(\hat{\mathbf{r}}) d\hat{\mathbf{r}}. \tag{26}$$

The electron-electron repulsion is again represented by its multipole expansion. Substituting these expressions into the two-electron matrix element of Eq. (24) gives

$$\langle G_i G_j | \chi_k^c \chi_l^d \rangle = \sum_{\lambda,\mu} \frac{4\pi(-1)^\mu}{2\lambda+1} \int R_{\lambda,-\mu}^{i,\ell^c,m^c}(r_1) \phi_k(r_1) \frac{r_<^\lambda}{r_>^{\lambda+1}}$$
$$\times R_{\lambda,\mu}^{j,\ell^d,m^d}(r_2) \phi_l(r_2) dr_1 dr_2. \tag{27}$$

We now follow the same procedure used in the preceding section, carrying out the integration over the first electron coordinate by solving an equivalent Poisson equation. Defining the densities,

$$\rho_1(r) \equiv R_{\lambda,-\mu}^{i,\ell^c,m^c}(r) \phi_k(r),$$

$$\rho_2(r) \equiv R_{\lambda,\mu}^{j,\ell^d,m^d}(r) \phi_l(r), \tag{28}$$

we can write

$$\langle G_i G_j | \chi_k^c \chi_l^d \rangle = \sum_{\lambda,\mu} \frac{4\pi(-1)^\mu}{2\lambda+1} = \left\langle \rho_1 \left| \frac{r_<^\lambda}{r_>^{\lambda+1}} \right| \rho_2 \right\rangle, \tag{29}$$

and proceeding as we did above gives

$$\left\langle \rho_1 \left| \frac{r_<^\lambda}{r_>^{\lambda+1}} \right| \rho_2 \right\rangle$$

$$= (2\lambda+1) \left(\frac{R_{\lambda,-\mu}^{i,\ell^c,m^c}(r_k)}{r_k} \frac{R_{\lambda,\mu}^{j,\ell^d,m^d}(r_l)}{r_l} \right) [T_{k,l}^\lambda]^{-1}$$

$$+ \left(\frac{r_0^{2\lambda+1} - r_l^{2\lambda+1}}{r_0^{2\lambda+1} - r_{max}^{2\lambda+1}} \right) \frac{R_{\lambda,-\mu}^{i,\ell^c,m^c}(r_k) R_{\lambda,\mu}^{j,\ell^d,m^d}(r_l) \sqrt{w_k w_l} r_k^\lambda}{r_l^{\lambda+1}}$$

$$+ \left(\frac{r_l^{2\lambda+1} - r_{max}^{2\lambda+1}}{r_0^{2\lambda+1} - r_{max}^{2\lambda+1}} \right) \frac{R_{\lambda,-\mu}^{i,\ell^c,m^c}(r_k) R_{\lambda,\mu}^{j,\ell^d,m^d}(r_l) \sqrt{w_k w_l} r_0^{2\lambda+1}}{(r_k r_l)^{\lambda+1}}. \tag{30}$$

This class of integrals requires the most computational effort of any of the hybrid two-electron integrals encountered. Note in particular that there is no fixed upper limit on the angular quantum numbers μ and λ in Eq. (27), so the upper limits must be determined empirically. The computational workload can be minimized by designing the hybrid basis to keep the Gaussians confined to as few DVR finite elements as possible. This will help to avoid having to evaluate many of these mixed-basis exchange integrals beyond the range of the Gaussian basis functions.

III. CONSTRUCTION OF THE HAMILTONIAN FOR Li$_2^+$

Equipped with the list of possible two-electron integrals that occur in a hybrid Gaussian–DVR basis, we turn our attention now to representing the Hamiltonian of Li$_2^+$ in this basis. The $^2\Sigma_g^+$ ground state of Li$_2^+$ is well represented by a single-configuration wave function $(1\sigma_g)^2(1\sigma_u)^2(2\sigma_g)$, representing a molecular system with one electron outside of a filled inner core. In order to consider photoionization of the valence electron, an accurate description of the interaction of this electron with those of the core is essential. The molecular orbitals that hold the core electrons are well described as plus or minus combinations of Li $1s$ atomic orbitals and can be accurately described by a few s-type GTOs centered on the nuclei. The core orbitals were obtained from a self-consistent-field (SCF) calculation on Li$_2^{++}$. The strategy was to represent the interaction of the valence electron with the closed-shell core via a nonlocal static exchange potential.

The effective one-electron Hamiltonian for the Li$_2^+$ molecule is (in atomic units)

$$H = T + V_{nuc} + 2J - K, \tag{31}$$

where

$$T = -\frac{1}{2}\nabla^2,$$

$$V_{nuc} = -\frac{Z}{|\mathbf{r} - \mathbf{A}|} - \frac{Z}{|\mathbf{r} + \mathbf{A}|}, \tag{32}$$

are the kinetic energy and nuclear attraction operators, respectively. The charge on each nuclei is $Z = 3$ with coordinates at each end of the molecular axis defined by $\mathbf{A}$. The repulsion of the valence electron with those constituting the core is given by the Coulomb and exchange operators $2J - K$, where

$$J(\mathbf{r}) = \int d\mathbf{r}' \frac{[1\sigma_g(\mathbf{r}')^2 + 1\sigma_u(\mathbf{r}')^2]}{|\mathbf{r} - \mathbf{r}'|} \tag{33}$$

and

$$K(\mathbf{r},\mathbf{r}')f(\mathbf{r}') = 1\sigma_g(\mathbf{r}) \int d\mathbf{r}' \frac{1\sigma_g(\mathbf{r}')f(\mathbf{r}')}{|\mathbf{r} - \mathbf{r}'|}$$
$$+ 1\sigma_u(\mathbf{r}) \int d\mathbf{r}' \frac{1\sigma_u(\mathbf{r}')f(\mathbf{r}')}{|\mathbf{r} - \mathbf{r}'|}. \tag{34}$$

The one-electron kinetic energy and nuclear attraction integrals in the hybrid representation were evaluated as in paper I, while the matrix elements of the core potential are expressed in terms of the appropriate two-electron integrals and the density matrix ρ for the occupied core,

$$\rho_{k,l} = [c_k^{1\sigma_g} c_l^{1\sigma_g} + c_k^{1\sigma_u} c_l^{1\sigma_u}]. \qquad (35)$$

where the c's are the expansion coefficients of the core orbitals constructed in a pure Gaussian basis. To represent the outer valence electron, the core Gaussian basis is augmented with additional Gaussian functions and the Coulomb operator is constructed as

$$\langle f_i | J | f_j \rangle = \sum_{k,l} \rho_{k,l} \langle f_i G_k | f_j G_l \rangle, \qquad (36)$$

where f_i and f_j are functions in the hybrid basis consisting of DVR functions and the augmented Gaussian basis, but the two-electron integral $\langle f_i G_k | f_j G_l \rangle$ involves only the core Gaussians indexed by k and l. Similarly, the exchange operator can be constructed using the density and various two electron integrals,

$$\langle f_i | K | f_j \rangle = \sum_{k,l} \rho_{k,l} \langle f_i G_k | G_l f_j \rangle. \qquad (37)$$

We note that this construction requires two-electron integrals of class 1 and class 3, but not class 2. Having outlined the computation of all integrals needed to construct a representation of Eq. (31) in a hybrid basis, we turn next to some illustrative calculations on Li_2^+.

IV. NUMERICAL TESTS OF THE BOUND STATES OF Li_2^+

Previous calculations [35–39] and experimental results [40,41] report the equilibrium bond distance of ground state Li_2^+ at $R \sim 5.9 a_0$, substantially larger than the bond distances of other covalently bonded diatomic molecules. Because of the design of the hybrid basis, the region inside of r_0 must be adequately described by only the Gaussian basis functions. The Gaussian basis set details utilized for the following calculations is displayed in Table I. The core orbitals were expanded in a set of three s-type contracted functions. These were obtained by contracting the first five and dropping the two most diffuse functions (with exponents 0.0767 and 0.286) from the $9s$ primitive set given by Dunning and Hay [29]. The augmented basis used to describe the valence electron includes GTOs with angular momentum contributions up to $l=3$ f-type functions. This basis was adequate for describing Li_2^+ at internuclear distances up to 6.0 bohr. The following results were robust to changes of the valence basis. The inclusion of more diffuse GTOs, including the addition of more Gaussians along the bond axis, did not change the results, indicating convergence of the inner region with this modest basis.

For the DVR portion of the hybrid basis, the radial grid started $0.1 a_0$ beyond the nuclei positions and employed radial finite elements at intervals of 5 bohr up to $r=20 a_0$, followed by three finite elements of 10 bohr leading up to the exterior complex scaling point $r_{ECS}=50 a_0$ and a 20 bohr complex decay element with ECS rotation angle $\eta=30°$. Within each finite element 17th-order DVR was used. The angular basis included spherical harmonics of the appropriate symmetry with $l_{max}=7$.

The calculation of the Li_2^+ potential energy curves of the ground and first few excited states are displayed in Fig. 2.

TABLE I. Gaussian basis function parameters for Li_2^+. The location of the Gaussian center is either on each atomic nuclei or at the center of the bond. The first three atomic s functions are used to build the core orbitals of the inner electrons; those that follow are used for the valence electron.

Location	Type	Exponent	Contraction coefficient
Atomic	s	921.3	0.002651
		138.7	0.020140
		31.94	0.096436
		9.353	0.310677
		3.158	0.666990
Atomic	s	1.157	1.0
Atomic	s	0.4446	1.0
Atomic	s	0.7	1.0
Atomic	s	0.2	1.0
Atomic	p	1.0	1.0
Atomic	p	0.5	1.0
Atomic	p	0.75	1.0
Atomic	p	0.1	1.0
Atomic	d	0.5	1.0
Center	s	0.1	1.0
Center	s	0.05	1.0
Center	p	0.3	1.0
Center	p	0.1	1.0
Center	d	0.1	1.0
Center	f	0.5	1.0

The solid lines are results from a previous calculation [42] while the corresponding symbols are results calculated using the hybrid basis at several internuclear distances. The agreement amongst these results and those of another model po-
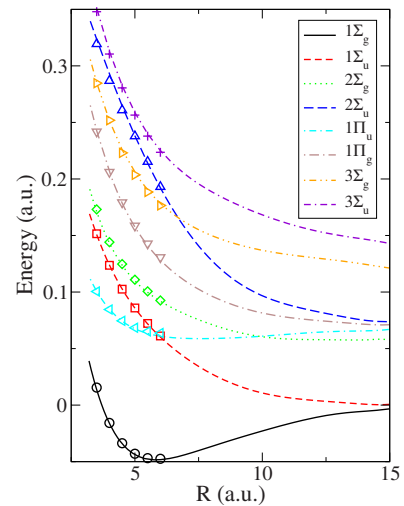

FIG. 2. (Color online) Potential energy curves of Li_2^+ for various symmetries. Solid curves are results of a previous *ab initio* calculation [42]. The corresponding discrete points are results calculated in the hybrid representation at internuclear distances from 3 to 6 bohr.

tential calculation [43] is excellent. The accuracy of the Rydberg state energies is a strong test of the completeness of the hybrid basis. The ground state minimum energy was calculated at $R=5.86a_0$, agreeing with these previous results. It should be noted that the DVRs are essential for accurately describing the first few excited states of Li_2^+, since the GTO list lacks diffuse functions. Indeed, calculations at $R=5.5a_0$ employing only the GTOs listed in Table I and no DVRs gave a 0.65 eV error for the $2\Sigma_g$ state and for the $3\Sigma_g$ state the error is more than 2 eV. The potential energy curves of Fig. 2 illustrate that the DVR portion of the hybrid basis is correctly connecting to the inner GTO region, accurately describing the Rydberg states of the molecule. This proper coupling between the components of the hybrid basis is essential to ensure that the physical space of the problem is adequately spanned by the full basis.

V. CALCULATION OF CONTINUUM STATES OF Li_2^+

A. Theoretical framework for evaluation of photoionization amplitudes

The results of Sec. IV confirm that the Hamiltonian constructed in Eq. (31) correctly describes the Li_2^+ system. The task now remains to construct the continuum states of Li_2^+ with outgoing electron momentum **k**. The details of this construction were given in paper I and will not be repeated here. We write the full wave function as

$$\Phi^{(+)}(\mathbf{k},\mathbf{r}) = \xi(\mathbf{k},\mathbf{r}) + g(r)\Psi_c^{(+)}(\mathbf{k},\mathbf{r}), \qquad (38)$$

where $\Psi_c^{(+)}(\mathbf{k},\mathbf{r})$ is an atomic Coulomb function with $Z=2$ representing the incoming part of the full solution, $g(r)$ is an arbitrary cutoff function that becomes unity at large distances and $\xi(\mathbf{k},\mathbf{r})$ is the unknown scattered wave. By expanding $\Psi_c^{(+)}(\mathbf{k},\mathbf{r})$ in partial waves and substituting Eq. (38) into the Schrödinger equation, one obtains driven equations

$$\left(\frac{k^2}{2} - H\right)\frac{\xi^{l_0,m}(\mathbf{r})}{r} = \left(H - \frac{k^2}{2}\right)g(r)\frac{\phi_{l_0,k}^{(c)}(r)}{r}Y_{l_0,m}(\hat{\mathbf{r}}) \quad (39)$$

for each partial wave component l_0,m of the Coulomb wave channel. By expanding $\xi^{l_0,m}(\mathbf{r})$ in the hybrid basis, Eq. (39) is converted to a set of linear equations for the unknown expansion coefficients. The cutoff function $g(r)$ must have continuous first and second derivatives and go to one for $r < r_{ECS}$, but is otherwise arbitrary. In this work, we choose $g(r)$ as

$$g(r) = \begin{cases} 0, & r < a, \\ 6x^5 - 15x^4 + 10x^3, & a \le r \le b, \\ 1, & r > b, \end{cases} \qquad (40)$$

where $x=(r-a)/(b-a)$. We generally choose a and b to coincide with finite element boundaries on the real portion of the grid and verified that for $a > 20$ bohr, the results were independent of the choice. By choosing $g(r)$ to be nonzero only beyond the range of the Gaussian basis functions, we eliminate the need for any matrix elements between GTOs and the Coulomb functions on the right-hand side of Eq. (39).
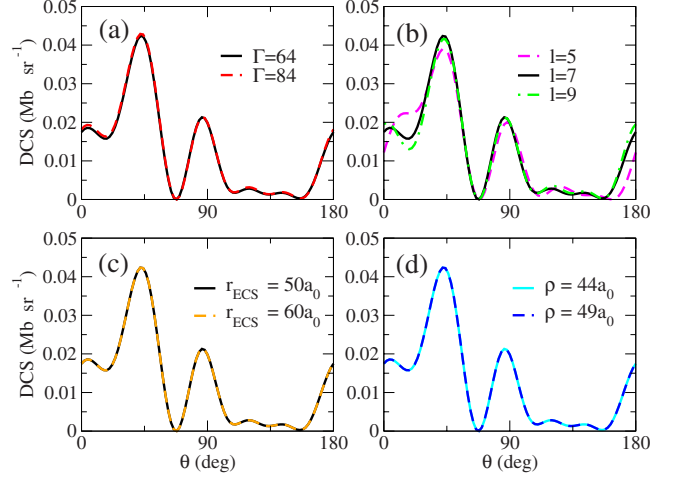

FIG. 3. (Color online) Convergence test of the hybrid method. Each panel displays angular photoionization cross sections of Li_2^+ at $R=5.86a_0$ with photon polarization 15° and 20 eV ejected electron energy. (a) Gaussian basis convergence demonstrated with additional f-type functions. Γ refers to the total number of contracted Gaussian functions in the basis. (b) Convergence of results with higher partial waves in the DVR angular basis. (c) Stability of results with larger radial DVR grid size. (d) Convergence of results with respect to the extraction surface location inside of r_{ECS}.

The photoionization amplitude for a fixed-in-space molecular orientation is defined by

$$\langle\Phi^{(-)}(\mathbf{k},\mathbf{r})|\epsilon\cdot\mathbf{r}|\Phi_0(\mathbf{r})\rangle,$$

where **k** is the outgoing electron momentum, $\Phi_0(\mathbf{r})$ is the initial state with energy E_0, $\epsilon\cdot\mathbf{r}$ is the dipole operator for a photon with polarization direction ϵ and energy ω and the final state $\Phi^{(-)}(\mathbf{k},\mathbf{r})$ is related to the function in Eq. (38) by

$$\Phi^{(-)}(\mathbf{k},\mathbf{r}) = [\Phi^{(+)}(-\mathbf{k},\mathbf{r})]^*. \qquad (41)$$

The photoionization amplitude can be computed from the solution of the perturbative first-order equation

$$[E_0 + \omega - H]\Psi_{sc} = (\epsilon\cdot\mathbf{r})\Psi_0, \qquad (42)$$

by writing

$$\langle\Phi^{(-)}(\mathbf{k},\mathbf{r})|\epsilon\cdot\mathbf{r}|\Phi_0(\mathbf{r})\rangle$$
$$= \langle\Phi^{(-)}(\mathbf{k},\mathbf{r})|(E-H)(E-H+i\epsilon)^{-1}\epsilon\cdot\mathbf{r}|\Phi_0(\mathbf{r})\rangle$$
$$= \langle\Phi^{(-)}(\mathbf{k},\mathbf{r})|E-H|\Psi_{sc}(\mathbf{r})\rangle. \qquad (43)$$

As described in paper I, this amplitude can be converted to a surface integral using Green's theorem. Moveover, by placing the surface well outside the range of the Gaussians and just inside the complex turning point r_{ECS}, we need only include DVR contributions from $\Phi^{(-)}(\mathbf{k},\mathbf{r})$ and Ψ_{sc}.

B. Convergence tests

Having outlined the tools necessary to evaluate cross sections for photoionization of Li_2^+, we next test the robustness of the method. Figure 3 shows the behavior of the differential cross section at 20 eV ejected photoelectron energy with
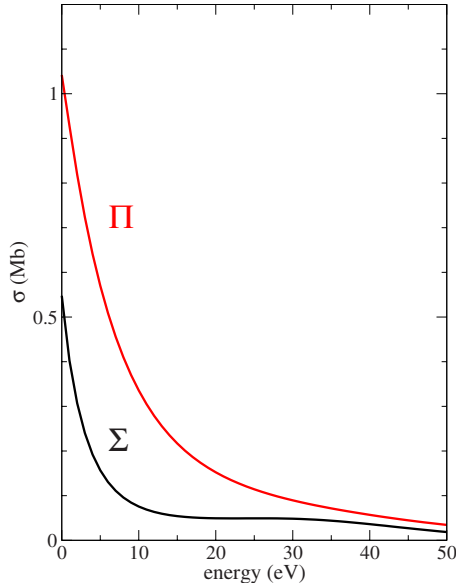
FIG. 4. (Color online) Total photoionization cross section of $Li_2{}^+$ versus ejected photoelectron energy. Lower curve: Photon polarization parallel to the molecular axis. Upper curve: Photon polarization perpendicular to the molecular axis.

a linearly polarized photon direction 15° relative to the molecular axis (at $R = 5.86 a_0$) as various parameters are varied. All angles are measured relative to the molecular axis throughout the following examples. Panel (a) displays the results derived using different inner region Gaussian basis sets. The solid curve was obtained using the GTO basis in Table I. Augmentation of the basis with additional f-type functions placed along the bond axis yields the broken curve, indicating that the inner region is adequately spanned by this basis. Panel (b) displays the convergence of the results with respect to the number of angular terms in the DVR basis. The results also show convergence is essentially reached by including partial waves up to $l_{max} = 7$, with the angular distribution only slightly altered by adding partial waves up to $l_{max} = 9$. Panels (c) and (d) indicate robustness of the results with respect to the radial DVR basis details. Neither the addition of another real finite element changing the radial grid size, nor a change in the extraction surface radius is seen to appreciably change the results. These tests indicate that these calculations are completely converged with respect to the parameters of the calculation.

VI. COMPUTED PHOTOIONIZATION CROSS SECTIONS OF $Li_2{}^+$

A. Total cross sections

A plot of the total photoionization cross section at equilibrium geometry at various photoelectron energies is shown in Fig. 4. The lower curve displays results for pure Σ polarization while the upper curve results are for the pure Π case. The total cross sections were calculated via two methods: By integrating the differential cross section over all angles and by evaluating the optical theorem expression

TABLE II. Comparison of the total photoionization cross sections for $Li_2{}^+$ calculated using both the optical theorem and integrating the differential cross section. Results are shown at various photoelectron energies for photon polarizations both parallel and perpendicular to the molecule.

		σ_{tot} (Mb)	
	Energy (eV)	Optical theorem	Integral
Σ	5	0.1567962	0.1567961
	10	0.0755934	0.0755954
	15	0.0540898	0.0540892
	20	0.0493177	0.0493171
Π	5	0.5701969	0.5701905
	10	0.3355458	0.3355456
	15	0.2168718	0.2168742
	20	0.1522864	0.1522889

$$\sigma_{tot} = \frac{4\pi\omega}{c} \, \text{Im} \langle \Psi_0 | \epsilon \cdot \mathbf{r} | \Psi_{sc} \rangle. \qquad (44)$$

Table II compares the numerical values of the total cross section calculated using these two methods at different energies and in different symmetries. The agreement of the results is excellent, providing further confirmation that the calculations are sufficiently converged.

It is interesting to note the striking differences in the total cross sections for $H_2{}^+$ and $Li_2{}^+$. The Σ component in $Li_2{}^+$ decreases monotonically from threshold, while in $H_2{}^+$ it rises to a maximum near 1 eV photoelectron energy and then decreases. Moreover, the ratio of Π to Σ at low energies is much larger for $H_2{}^+$ than for $Li_2{}^+$. This ratio is $\sim$6 in $H_2{}^+$ at 1 eV, while in $Li_2{}^+$, the ratio is close to 2 near threshold.

B. Angular distributions at 10 eV

To illustrate the detailed information of molecular photoionization calculated in the hybrid scheme, the differential cross sections (DCS) for photoionization from $Li_2{}^+$ with internuclear distance $R = 5.86 a_0$ are shown in the following sections. Figure 5 considers the case for 10 eV photoelectron energy. The cross sections display a more complex angular distribution than those observed for $H_2{}^+$ with internuclear separation $R = 2.0 a_0$ for the same photoelectron energy [9,14]. The larger internuclear distance appears to give angular distributions different from the more spherical $H_2{}^+$ molecule, whose angular distributions at 10 eV appear more atomiclike.

While the shape of the DCS in Fig. 5 is similar to $H_2{}^+$ for pure Σ polarization results, the angular distributions for other polarizations are more complicated. In particular, the pure Π polarization case gives an angular distribution with three lobes reminiscent of classical interference patterns from double-slit experiments. Such phenomena have been studied in $H_2{}^+$ [6,44] and H_2 [45], requiring a significantly larger photoelectron energy to make the electron wavelength comparable to the internuclear separation [46]. However, with
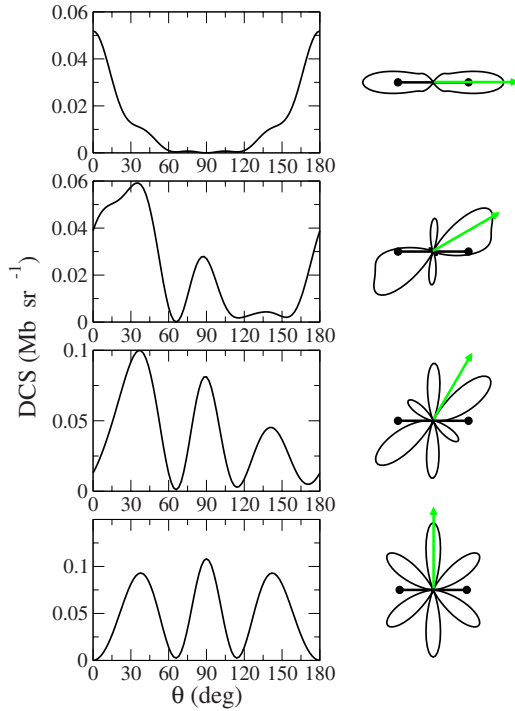
FIG. 5. (Color online) Differential cross sections and angular distributions for photoionization of Li_2^+ at $R=5.86a_0$ ejecting a 10 eV photoelectron. The polarization vector is $\varphi=0°$, $30°$, $60°$, and $90°$ from top to bottom. The relative angular distributions are shown beside the absolute cross sections with the polarization vector (single-pointed arrow) measured from the molecular axis.

such a large equilibrium internuclear separation in Li_2^+, the photoelectron wavelength becomes comparable to the bond distance at much lower energies. The de Broglie wavelength for a 10 eV photoelectron is $\lambda_e \sim 7.3a_0$, making the energy ranges for observing classical interference effects in the angular distributions more accessible for the long bond length of Li_2^+ compared to smaller molecules.

C. Angular distributions at 2 eV

To further investigate the interplay of the nuclear geometry and possible interference effects in the photoionization differential cross sections, we move to an energy near threshold where the photoelectron possesses a longer wavelength λ_e. At 2 eV, this wavelength is $\sim 16.4a_0$, significantly longer than the $R=5.86a_0$ Li_2^+ bond distance. Thus, the possibility of double-slit interference effects impacting the angular distributions is significantly diminished at this lower ejection energy. Differential cross sections and relative angular distribution plots for this case are shown in Fig. 6.

The angular distribution in the perpendicular polarization case again shows a three-lobe structure, indicating a significant contribution from the $l=3$ f-wave component to the outgoing wave function. Figure 7 plots the real part of the outgoing $\Psi_{sc}(\mathbf{r})$ in the xz plane for pure Π polarization. The lobes in the cross section have their origins in the visible jets of outgoing amplitude in the wave function. By analyzing the partial-wave T-matrix elements of the scattered wave
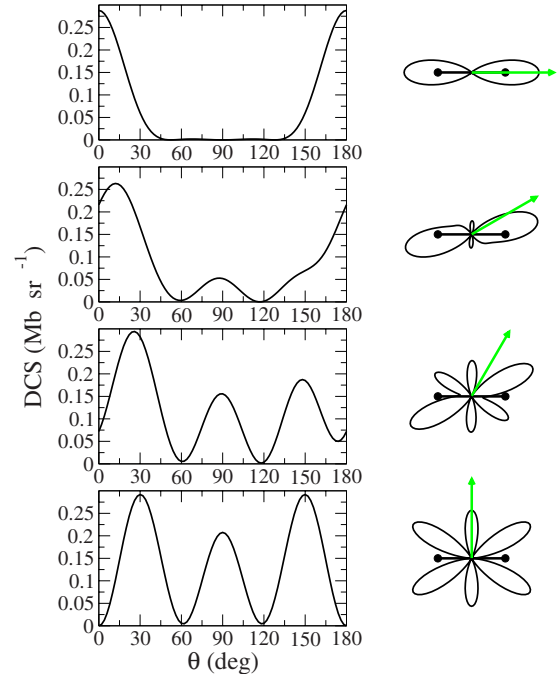

FIG. 6. (Color online) Differential cross sections and angular distributions for photoionization of Li_2^+ at $R=5.86a_0$ ejecting a 2 eV photoelectron, with polarization $\varphi=0°$, $30°$, $60°$, and $90°$ from top to bottom. Even at this low energy, the angular distributions do not appear as atomiclike as observed for less severely nonspherical diatomics like H_2^+, indicating the contribution of higher partial wave components closer to the photoionization threshold for longer bond distances.

function, as we did in paper I, we found that the f-wave contributes significantly to the outgoing wave function even at 2 eV above the photoionization threshold for both polarizations parallel and perpendicular to the molecular axis. In contrast to H_2^+ at $R=2.0a_0$, the significantly larger internuclear separation of Li_2^+ represents an equilibrium geometry vastly more nonspherical, thereby introducing higher angular momentum components into the wave function. These higher partial waves impact the angular distributions at much lower energies for large internuclear separations relative to more spherically shaped diatomic molecules. Thus, what appears to be a double-slit interference effect in the angular distributions for near-threshold photoionization is more likely attributed to the importance of higher angular momentum terms for severely nonspherical molecular target geometries.

D. Angular distributions at 20 eV

Finally, turning to a higher energy range readmits the possibility of interference effects between the ejected photoelectron and the target. Figure 8 displays angular cross sections for photoionization of Li_2^+ for a 20 eV photoelectron. The corresponding de Broglie wavelength of the electron is ~ 5.2 bohr, slightly smaller than the internuclear separation.

In this case, we expect interferencelike structures to be more evident than the previous results at 10 eV. Figure 9 compares the three-dimensional cross sections for these two photoelectron energies with parallel and perpendicular polar-
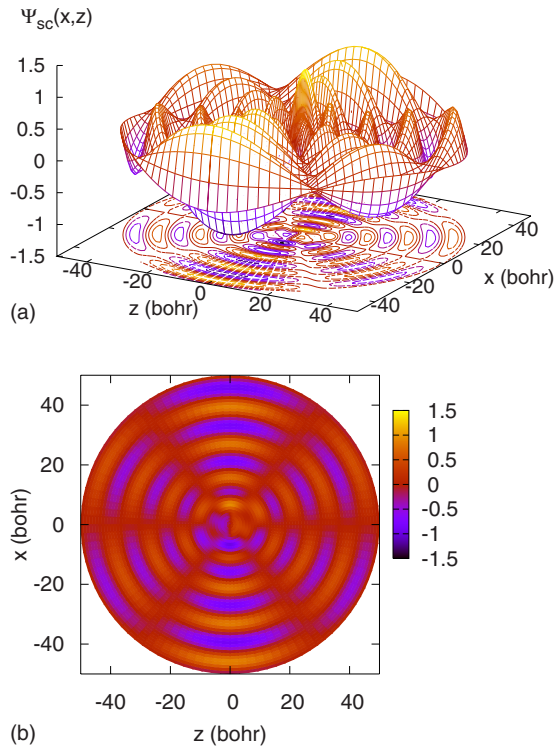
(a)

(b)

FIG. 7. (Color online) Upper panel: Real part of the outgoing scattered wave function $\Psi_{sc}(\mathbf{r})$ in Π_u symmetry plotted above the xz plane. Lower panel: Contour plot of the above wave function projected in the xz plane. The angular distribution of the $\varphi = 90°$ polarization in Fig. 6 correlates to the directions of outgoing amplitude in the scattered wave, indicating stronger contribution from the $l=3$ partial wave than is observed for H_2^+ at equilibrium geometry.

izations. Indeed, a comparison of the pure Σ polarization angular distributions reveals that the higher energy photon leads to more prominent structure in directions off the molecular axis, with distinct lobes emerging in going from 10 eV to 20 eV. Furthermore, the perpendicular polarization angular distributions at these energies exhibit the expected behavior of a double-slit interference result as the energy is increased. The peaks symmetric with the main peak along the polarization axis are observed to move closer to the central peak, with all lobes becoming more sharply defined about their maxima. The corresponding minima also move towards the polarization direction as expected.

The examples at polarization directions $\varphi = 30°$ and $\varphi = 60°$ also change consistent with what would be expected for an interference pattern as the photoelectron wavelength is shortened from Fig. 5 to Fig. 8, with lobes becoming sharper and more defined as the energy is increased. In summary, the angular distributions of cases where the photoelectron wavelength λ_e becomes comparable to the large bond distance of Li_2^+ begin to display interference characteristics for photon energies lower than are required to produce such effects for diatomic systems with shorter bond lengths.

VII. CONCLUSIONS

The hybrid representation derives its attractiveness for use in treating continuum problems involving molecular targets
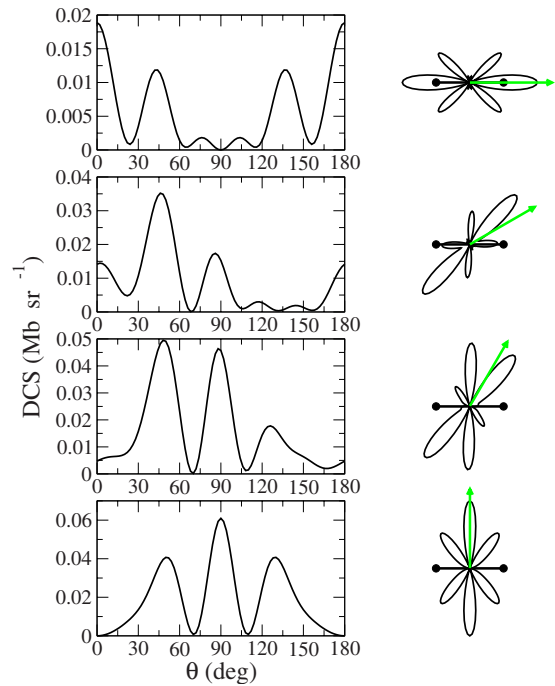

FIG. 8. (Color online) Differential cross sections and angular distributions for photoionization of Li_2^+ at $R = 5.86a_0$ ejecting a 20 eV photoelectron, with polarization vector $\varphi = 0°$, $30°$, $60°$, and $90°$ from top to bottom. At this higher photoelectron energy, the appearance of interference phenomena is more markedly observed than in the lower energy cases.

by combining the advantageous qualities of its component basis sets. Simultaneously harnessing both the ability of analytic Gaussian-type basis functions to describe electronic coordinates near the nuclei in bound orbitals and the power of grid-based DVR methods employing exterior complex scaling for description of continuum electronic coordinates renders the hybrid basis suitable for molecular photoionization
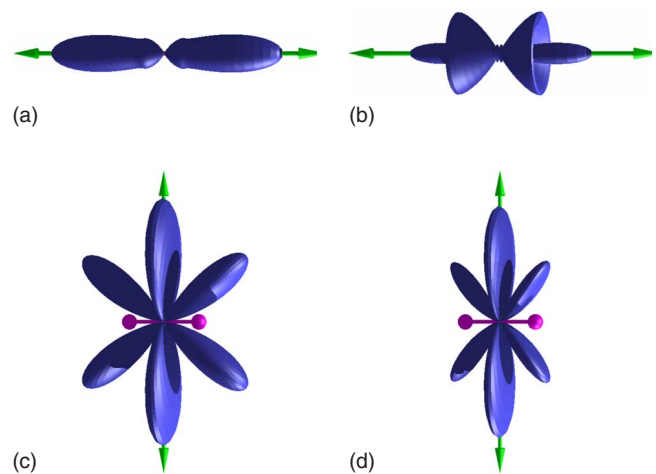

(a)   (b)

(c)   (d)

FIG. 9. (Color online) Three-dimensional angular distributions of the photoelectron from Li_2^+ with energies of 10 eV (left-hand column) and 20 eV (right-hand column). Results with Σ polarization are on the upper row, Π polarization on the lower row. The changes in the cross section shapes as the photoelectron energy is raised are consistent with the behavior of interference phenomena.

problems. This marriage of both bound state basis set methods and grid-based technologies capitalizes on the decades of research and refinement that have been spent to improve and optimize both constituent components.

The hybrid method has been extended beyond the evaluation of one-electron operators with the complete catalog of possible two-electron integrals that occur in this scheme tabulated in Sec. II C. These classes of two-electron integrals differ in the possible combinations of Gaussians or DVR-type functions among the four indices and are evaluated according to the properties of the component bases. The overall basis is designed to minimize the number of these two-electron integrals that need to be evaluated.

The method has been successfully applied to treat photo-ionization of Li_2^+, where the large equilibrium internuclear distance would complicate a purely single-center approach with existing grid-based formulations. This large bond distance leads to interesting consequences in the angular distributions of the computed cross sections, namely the large contribution from higher angular momentum components even at low photoelectron energies and the appearance of

double-slit interference phenomena at energies above 10 eV.

Since the manifestations of molecular interference phenomena appear similar to the near-threshold behavior of the angular distributions that is a consequence of the nonspherical molecular geometry, it is difficult to pinpoint exactly at what energies the observed angular patterns in the cross sections are dominated by interference effects alone. Indeed, the role of internuclear separation on the angular structure arising from the interplay between molecular geometry and interference effects when energetically possible remains an interesting topic requiring further investigation.

[1] M. Foster and J. Colgan, J. Phys. B **39**, 5067 (2006).

[2] C. W. McCurdy, D. A. Horner, T. N. Rescigno, and F. Martín, Phys. Rev. A **69**, 032707 (2004).

[3] F. L. Yip, D. A. Horner, C. W. McCurdy, and T. N. Rescigno, Phys. Rev. A **75**, 042715 (2007).

[4] A. Palacios, C. W. McCurdy, and T. N. Rescigno, Phys. Rev. A **76**, 043420 (2007).

[5] D. A. Horner, F. Morales, T. N. Rescigno, F. Martin, and C. W. McCurdy, Phys. Rev. A **76**, 030701(R) (2007).

[6] J. Fernandez, O. Fojon, A. Palacios, and F. Martin, Phys. Rev. Lett. **98**, 043005 (2007).

[7] S. Selsto, A. Palacios, J. Fernandez, and F. Martin, Phys. Rev. A **75**, 033419 (2007).

[8] R. DellaPicca, P. D. Fainstein, M. L. Martiarena, and A. Dubois, Phys. Rev. A **75**, 032710 (2007).

[9] M. Foster, J. Colgan, O. Al-Hagan, J. L. Peacher, D. H. Madison, and M. S. Pindzola, Phys. Rev. A **75**, 062707 (2007).

[10] J. Colgan, M. Foster, M. S. Pindzola, and F. Robicheaux, J. Phys. B **40**, 4391 (2007).

[11] W. Vanroose, F. Martin, T. N. Rescigno, and C. W. McCurdy, Phys. Rev. A **70**, 050703(R) (2004).

[12] W. Vanroose, F. Martín, T. N. Rescigno, and C. W. McCurdy, Science **310**, 1787 (2005).

[13] W. Vanroose, D. A. Horner, F. Martín, T. N. Rescigno, and C. W. McCurdy, Phys. Rev. A **74**, 052702 (2006).

[14] T. N. Rescigno, D. A. Horner, F. L. Yip, and C. W. McCurdy, Phys. Rev. A **72**, 052709 (2005), referred to as paper I.

[15] M. R. H. Rudge and M. J. Seaton, Proc. R. Soc. London, Ser. A **283**, 262 (1965).

[16] M. R. H. Rudge, Rev. Mod. Phys. **40**, 564 (1968).

[17] P. J. Marchalant and K. Bartschat, Phys. Rev. A **56**, R1697 (1997).

[18] F. Maulbetsch and J. S. Briggs, J. Phys. B **26**, 1679 (1993).

[19] J. Berakdar and J. S. Briggs, Phys. Rev. Lett. **72**, 3799 (1994).

[20] I. Bray, Phys. Rev. Lett. **78**, 4721 (1997).

[21] A. Kheifets and I. Bray, J. Phys. B **31**, L447 (1998).

[22] P. Selles, L. Malegat, and A. K. Kazansky, Phys. Rev. A **65**, 032711 (2002).

[23] M. S. Pindzola *et al.*, J. Phys. B **40**, R39 (2007).

[24] M. Pont and R. Shakeshaft, Phys. Rev. A **51**, 494 (1995).

[25] C. W. McCurdy, M. Baertschy, and T. N. Rescigno, J. Phys. B **37**, R137 (2004).

[26] C. A. Nicolaides and D. R. Beck, Phys. Lett. **65**, 11 (1978).

[27] B. Simon, Phys. Lett. **71**, 211 (1979).

[28] T. N. Rescigno and C. W. McCurdy, Phys. Rev. A **62**, 032706 (2000).

[29] T. H. Dunning and P. J. Hay, in *Modern Theoretical Chemistry*, edited by H. F. Schaefer III (Plenum, New York, 1977), Vol. 3, pp. 1–28.

[30] J. V. Lill, G. A. Parker, and J. C. Light, Chem. Phys. Lett. **89**, 483 (1982).

[31] D. E. Manolopoulos and R. E. Wyatt, Chem. Phys. Lett. **152**, 23 (1988).

[32] I. Shavitt, in *Methods in Computational Physics*, edited by B. Alder, S. Fernbach, and M. Rotenberg (Academic, New York, 1963), pp. 1–45.

[33] V. I. Lebedev and D. N. Laikov, Dokl. Math. **59**, 477 (1999).

[34] J. A. Gaunt, Philos. Trans. R. Soc. London, Ser. A **228**, 151 (1929).

[35] P. Fuentealba, H. Preuss, H. Stoll, and L. V. Szentpály, Chem. Phys. Lett. **89**, 418 (1982).

[36] W. Müller and M. Jungen, Chem. Phys. Lett. **40**, 199 (1976).

[37] D. D. Konowalow and M. E. Rosenkrantz, Chem. Phys. Lett. **61**, 489 (1979).

[38] D. D. Konowalow and J. L. Fish, Chem. Phys. Lett. **104**, 210 (1984).

[39] C. Bottcher and A. Dalgarno, Chem. Phys. Lett. **36**, 137 (1975).

[40] R. A. Bernheim, L. P. Gold, and T. Tipton, Chem. Phys. Lett. **92**, 13 (1982).

[41] R. A. Bernheim, L. P. Gold, T. Tipton, and D. D. Konowalow, Chem. Phys. Lett. **105**, 201 (1984).

[42] I. Schmidt-Mink, W. Müller, and W. Meyer, Chem. Phys. **92**, 263 (1985).

[43] S. Magnier, S. Rousseau, A. R. Alloche, G. Hadinger, and M. Aubert-Frécon, Chem. Phys. **246**, 57 (1999).

[44] R. DellaPicca, P. D. Fainstein, M. L. Martiarena, and A. Dubois, Phys. Rev. A **75**, 032710 (2007).

[45] D. Akoury *et al.*, Science **318**, 949 (2007).

[46] H. Cohen and U. Fano, Phys. Rev. **150**, 30 (1966).